OPEN ACCESS

Environment & Ecology ARTICLE

The Innovation Geoscience

Soil moisture deficits amplify and prolong vegetation productivity losses under compound dry-hot extremes

Shuzhe Huang,[1,2] Siqi Wang,[3,*] Chao Wang,[1] Xiang Zhang,[4] Jianya Gong,[1,5,*] and Nengcheng Chen[4,6,*]

*Correspondence: wangsiqi@hubu.edu.cn (S.W.); gongjy@whu.edu.cn (J.G.); chennengcheng@cug.edu.cn (N.C.)

Received: January 19, 2026; Accepted: June 1, 2026; Published Online: June 3, 2026; https://doi.org/10.59717/j.xinn-geo.2026.100235

GRAPHICAL ABSTRACT

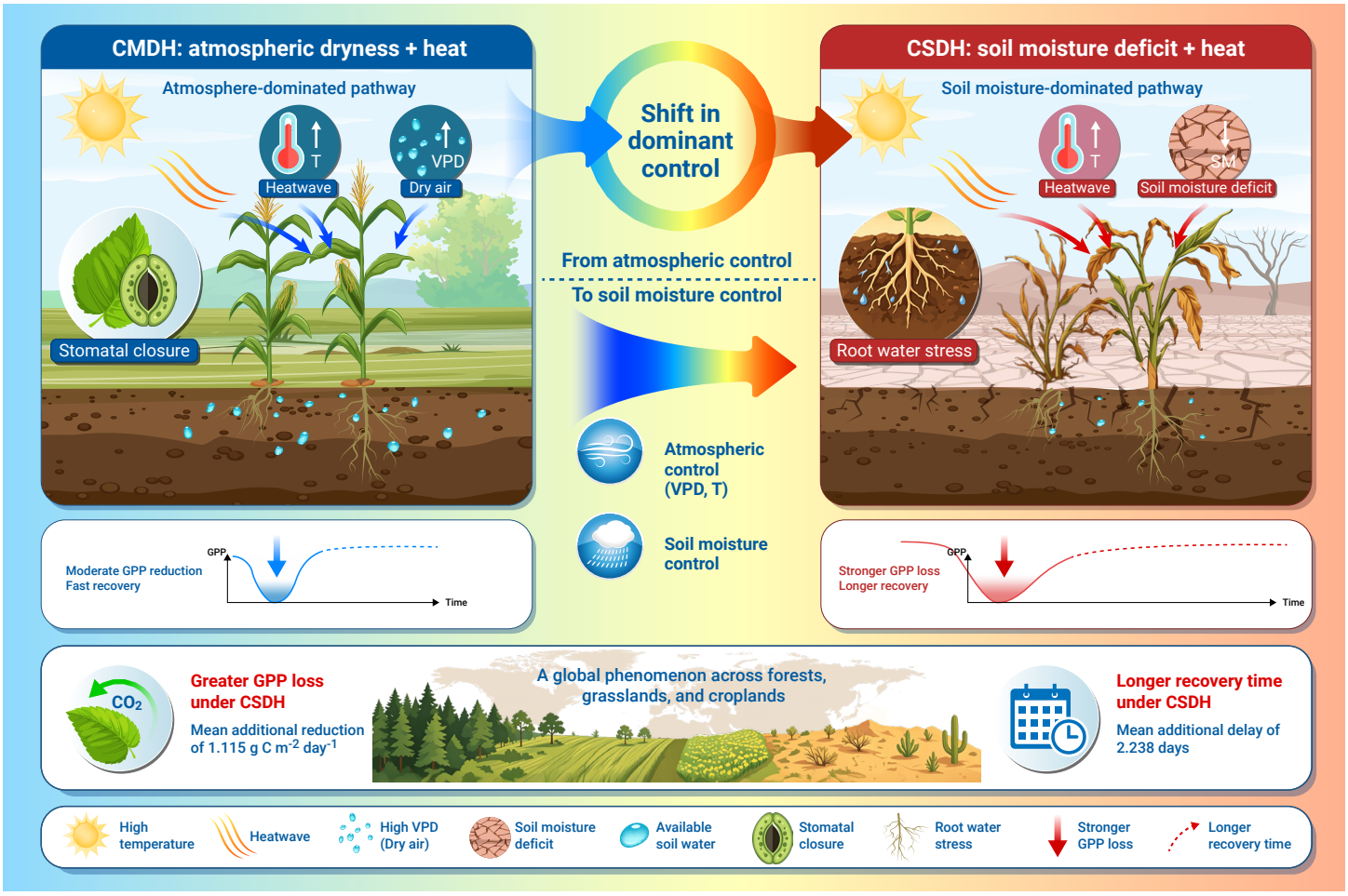

PUBLIC SUMMARY

- Soil-driven dry-hot events cause deeper GPP loss (−1.115 g·C·m^{-2}·day^{-1}) and slower recovery (+2.238 days).
- Impacts of soil moisture deficits intensify over time, widening divergence from atmospheric-driven events.
- Soil moisture control strengthens with event severity, aridity, and future warming scenarios.

ARTICLE Environment & Ecology

OPEN ACCESS

www.the-innovation.org/the-innovation-geoscience

Soil moisture deficits amplify and prolong vegetation productivity losses under compound dry-hot extremes

Shuzhe Huang,[1,2] Siqi Wang,[3,*] Chao Wang,[1] Xiang Zhang,[4] Jianya Gong,[1,5,*] and Nengcheng Chen[4,6,*]

[1]State Key Laboratory of Information Engineering in Surveying, Mapping, and Remote Sensing (LIESMARS), Wuhan University, Wuhan 430079, China

[2]State Key Laboratory of Resources and Environmental Information System, Institute of Geographic Sciences and Natural Resources Research, Chinese Academy of Sciences, Beijing 100101, China

[3]School of Artificial Intelligence, Hubei University, Wuhan 430062, China

[4]National Engineering Research Center of Geographic Information System, School of Geography and Information Engineering, China University of Geosciences (Wuhan), Wuhan 430074, China

[5]School of Remote Sensing and Information Engineering, Wuhan University, Wuhan 430079, China

[6]Hubei Luojia Laboratory, Wuhan 430079, China

*Correspondence: wangsiqi@hubu.edu.cn (S.W.); gongjy@whu.edu.cn (J.G.); chennengcheng@cug.edu.cn (N.C.)

Received: January 19, 2026; Accepted: June 1, 2026; Published Online: June 3, 2026; https://doi.org/10.59717/j.xinn-geo.2026.100235

Citation: Huang S., Wang S., Wang C., et al. (2026). Soil moisture deficits amplify and prolong vegetation productivity losses under compound dry-hot extremes. *The Innovation Geoscience* **4**:100235.

Compound dry-hot extremes have emerged as a major threat to terrestrial ecosystem productivity under climate change, yet their impacts are commonly interpreted through atmospheric conditions alone. Here we distinguish between compound meteorological dry-hot (CMDH) events, driven by atmospheric dryness and heat, and compound soil dry-hot (CSDH) events, in which soil moisture deficits coincide with heat, and assess their differential effects on global vegetation productivity. Integrating multiple gross primary productivity (GPP) datasets with climate variables, we quantify GPP loss and recovery time following CMDH and CSDH events. Globally, CSDH causes deeper productivity losses than CMDH, with a mean additional reduction of 1.115 $g{\cdot}C{\cdot}m^{-2}{\cdot}day^{-1}$, and prolongs recovery by 2.238 days on average. These differences have intensified over recent decades, with CSDH-related GPP losses and recovery times diverging increasingly from CMDH. The dominance of soil-driven impacts is also shown to strengthen with event severity, climate aridity, and under future warming scenarios. Structural equation modeling and explainable machine learning further reveal a shift in controlling mechanisms from atmospheric demand under CMDH to soil moisture limitation under CSDH, explaining both deeper carbon losses and longer ecosystem memory. Our results demonstrate that soil-coupled compound dry-hot extremes exert a more persistent constraint on terrestrial productivity than atmospheric counterparts, highlighting soil moisture as a critical regulator of ecosystem resilience in a warming world.

INTRODUCTION

Terrestrial vegetation productivity plays a central role in regulating the global carbon cycle, land-atmosphere energy exchange, and ecosystem resilience under climate change.[1-3] As the primary biological pathway for carbon uptake, gross primary productivity (GPP) integrates the combined effects of climate variability, water availability, and physiological stress on vegetation functioning.[4,5] Over recent decades, accelerating global warming has fundamentally altered the hydroclimatic background under which ecosystems operate, amplifying the frequency, intensity, and spatial extent of droughts and heat extremes.[6-8] These changes have raised growing concern about the stability of terrestrial carbon sinks and the capacity of ecosystems to withstand and recover from climate stress.[9-11]

A defining feature of contemporary climate extremes is the increasing prevalence of compound events, in which multiple stressors co-occur or interact in ways that produce impacts exceeding those expected from individual hazards alone.[12,13] Among these, compound dry-hot events have emerged as particularly consequential for vegetation productivity, as high temperatures intensify atmospheric water demand while drought constrains soil water supply.[14-16] Observational and modeling studies have shown that compound dry-hot conditions can trigger disproportionately large reductions in photosynthesis, elevate plant mortality risks, and disrupt post-disturbance recovery processes.[17,18] These impacts are not simply additive, instead, they reflect nonlinear interactions between atmospheric demand, soil moisture constraints, and plant physiological regulation.

Despite rapid advances in the study of compound climate extremes, a critical distinction within dry-hot events has received limited systematic attention, namely the contrast between compound meteorological dry-hot events (CMDH), which are dominated by atmospheric dryness and heat, and compound soil dry-hot events (CSDH), in which soil moisture deficits coincide with high temperatures. Meteorological drought and soil drought are often treated interchangeably in large-scale assessments, yet they represent fundamentally different modes of water stress.[19,20] Atmospheric dryness, commonly characterized by elevated vapor pressure deficit (VPD), primarily regulates stomatal conductance and short-term photosynthetic suppression, whereas soil moisture deficits exert stronger control over root water uptake, hydraulic integrity, and longer-term ecosystem memory.[11,21,22] When coupled with heat extremes, these two drought pathways may generate contrasting patterns of productivity loss and recovery, with important implications for ecosystem resilience.

Recent advances in the study of dry-hot extremes have expanded the focus beyond productivity losses during events to include post-event vegetation recovery, recognizing recovery as an integral component of ecosystem response to climate stress.[23-25] Recovery dynamics are increasingly acknowledged as a key factor shaping cumulative carbon impacts, legacy effects, and ecosystem sensitivity to recurrent extremes.[26] Within this growing body of work, dry-hot extremes are commonly examined as an integrated stressor, while the underlying pathways through which atmospheric and soil moisture constraints influence recovery are not always explicitly differentiated. Some studies emphasize the role of elevated vapor pressure deficit in prolonging recovery under hot and dry conditions, particularly in water-limited ecosystems, whereas others highlight soil moisture legacies as the dominant control on post-drought carbon uptake.[27,28] Rather than being contradictory, these perspectives point to complementary mechanisms and motivate a clearer separation of atmospheric and soil drought pathways when assessing both productivity loss and recovery under compound dry-hot extremes.

Addressing this question requires moving beyond comparisons between compound and single extremes, toward a framework that explicitly contrasts soil-driven and atmosphere-driven compound stress.[29,30] Such a distinction is especially relevant under ongoing climate change. Rising temperatures are projected to increase VPD globally, even in regions where precipitation trends remain uncertain, while soil moisture responses are shaped by slower hydrological processes and land-surface feedbacks.[31,32] Understanding how these pathways differentially affect vegetation productivity is essential for anticipating future carbon-climate feedbacks, particularly as ecosystems face increasingly frequent sequences of extreme events with limited recovery windows.

To address these unresolved questions, this study conducts a comprehensive global assessment of vegetation productivity responses to CMDH and CSDH events. By integrating multiple satellite-derived GPP products with reanalysis-based climate variables and soil moisture observations, we systematically quantify differences in GPP loss and recovery time between

these two types of compound extremes across space, climate zones, vegetation types, and event intensities. We further examine how these differences have evolved over recent decades and how they may change under future warming scenarios using multiple Shared Socioeconomic Pathways. To elucidate the underlying drivers, we combine structural equation modeling with explainable machine learning approaches, enabling a process-oriented interpretation of how atmospheric demand, soil water availability, and associated climatic factors jointly regulate ecosystem productivity under compound stress. Through this framework, the study aims to clarify the distinct roles of soil and atmospheric drought pathways in shaping ecosystem vulnerability and resilience to compound dry-hot extremes in a warming world.

MATERIALS AND METHODS

Data

The primary dataset used in this study is a global daily GPP product simulated by the Boreal Ecosystem Productivity Simulator (BEPS-GPP; 0.072727°) for 1980-2019.[33] BEPS is a process-based terrestrial biosphere model that integrates canopy photosynthesis, energy balance, hydrological processes, and soil biogeochemistry to represent ecosystem carbon uptake. This dataset was used to identify compound dry-hot events and quantify associated GPP loss and recovery.

To assess the robustness, four additional GPP products were analyzed. The MODIS and FLUXNET-derived GPP product (MODIS-GPP; daily and 0.05° from 2000-2020) provides global estimates based on machine-learning upscaling of eddy covariance observations.[34] Three additional satellite-based products were used at coarser temporal resolution, including GOSIF-GPP (8-day, 0.05°, 2000-2020) derived from solar-induced fluorescence, VOD-GPP (8-day, 0.25°, 1988-2020) based on vegetation optical depth, and NIRv-GPP (monthly, 0.05°, 1982-2019) derived from near-infrared reflectance.[35-37] All products were resampled to a common 1° resolution. BEPS-GPP and MODIS-GPP were analyzed at daily scale, while the remaining products were aggregated and used at monthly resolution.

Meteorological and hydrological variables, including precipitation, soil moisture, temperature, radiation, and humidity, were derived from the ERA5-Land reanalysis, with vapor pressure deficit (VPD) calculated accordingly.[38] Future projections were obtained from ten CMIP6 models under four Shared Socioeconomic Pathways (SSP1-2.6, SSP2-4.5, SSP3-7.0, SSP5-8.5) using the multi-model ensemble mean. The information of applied CMIP6 models is shown in Table S1. All variables were resampled to 1° resolution. To assess the robustness of the projections, we quantified inter-model uncertainty using a signal-to-noise ratio (SNR) based on the CMIP6 multi-model ensemble (Text S1, Figure S1). Overall, SNR values are generally greater than 1 across most regions, indicating that the projected signals are stronger than inter-model spread.

To characterize heterogeneity, climate zones were defined using the Köppen-Geiger climate classification.[39] Aridity levels were derived from a global aridity index dataset, classifying regions into five categories from extremely arid to humid. The locations of climate zones and dry-humid areas can refer to Figure S2. Vegetation types were identified using the MODIS MCD12Q1 land cover product, enabling stratified analysis of ecosystem responses across major vegetation functional categories.

Identification of CMDH and CSDH events

Compound dry-hot events were classified into two categories based on drought pathways, namely compound meteorological dry-hot events and compound soil dry-hot events. CMDH events were defined using VPD, representing atmospheric water demand, whereas CSDH events were characterized by soil moisture deficits.

Following established frameworks for compound event identification, drought and heat extremes were identified using percentile-based thresholds.[40] Meteorological drought was defined as VPD exceeding the 85th percentile, while corresponded to soil moisture below the 15th percentile. Heat extremes were defined using a moving-window approach. For each calendar day, the 85th percentile threshold was computed from all daily maximum temperature (T_{max}) observations within a 15-day window (±7 days) centered on that day. A hot day was identified when T_{max} exceeded its 85th percentile threshold.[41] All thresholds were derived from the 1980-1999 reference period. A compound dry-hot event was recorded when drought and heat extremes co-occurred on the same day. The duration of each event was defined as the consecutive days of compound conditions. To avoid artificial fragmentation of prolonged events interrupted by brief respites, events separated by fewer than three days were merged unless interrupted by extreme precipitation (daily precipitation > 95th percentile), which terminated the drought phase.

We further classified compound dry-hot events into three severity categories based on combined drought and heat thresholds. Moderate events were defined by VPD or soil moisture percentiles between the 15th (85th) and 10th (90th) percentiles combined with T_{max} percentiles between the 85th and 90th. Heavy events were defined by percentiles between the 10th (90th) and 5th (95th) combined with T_{max} percentiles between the 90th and 95th, while extreme events were defined by percentiles exceeding the 5th (95th) threshold combined with T_{max} percentiles exceeding the 95th.

Calculation of GPP loss and recovery time under CMDH and CSDH

To quantify ecosystem responses to compound events, GPP time series were first detrended to remove long-term background changes. (Figure S3). Daily anomaly ($\Delta GPP_{i,d,y}$) for day d in year y at grid cell i was then computed relative to the climatological mean seasonal cycle:

$$\Delta GPP_{i,d,y} = GPP_{i,d,y} - \overline{GPP_{i,d}} \quad (1)$$

where $\overline{GPP_{i,d}}$ represents the climatological mean GPP for day d averaged. Negative GPP anomalies were identified using a dynamic threshold as $-0.5 \times \sigma_{GPP_{i,d}}$, where $\sigma_{GPP_{i,d}}$ denotes the standard deviation of GPP for day d at grid cell i over the study period. Days with $\Delta GPP_{i,d,y} \leq -0.5 \times \sigma_{GPP_{i,d}}$ were classified as experiencing vegetation anomalies, indicating productivity suppression exceeding half a standard deviation below the climatological expectation. Total GPP loss was calculated as the cumulative sum of daily anomalies during the event.

Recovery time was defined as days required for GPP to return above the threshold for at least five consecutive days.[42] This criterion distinguished recovery from transient rebounds that might be followed by renewed suppression due to legacy effects or secondary stressors. Vegetation was classified as still recovering if anomalies recurred within five days of the initial return to normal conditions. We also conducted a sensitivity analysis by testing additional recovery window thresholds of 3, 7, and 10 consecutive days, and the results show that the global spatial patterns of both GPP loss and recovery time remain highly consistent across different threshold settings (Figure S4).

To isolate the influence of individual compound events, we applied quality control filters to the recovery time estimates. First, we excluded events that did not produce any detectable negative GPP anomalies following their ending, as these reflected either absence of stress or mitigation mechanisms rendering post-event recovery metrics inapplicable. Second, we removed cases where vegetation exhibited anomalies that were not preceded by compound dry-hot conditions, ensuring that observed suppression was attributable to the focal event rather than unrelated disturbances. Third, we excluded samples that experienced two or more compound dry-hot events during the recovery period, as overlapping stressors would confound estimates by introducing additional suppression or prolonging recovery through cumulative legacy effects.

The resulting GPP loss and recovery time were then calculated separately for CMDH and CSDH events at each grid cell. As an additional sensitivity test, we calculated CMDH events using precipitation deficits instead of VPD as the meteorological drought indicator. The resulting spatial patterns of GPP loss and recovery time show high consistency with those derived from the VPD-based definition, with high correlations for both GPP loss (PCC = 0.93, $p < 0.01$) and recovery time (PCC = 0.73, $p < 0.01$) (Figure S5).

Sensitivity analysis of GPP loss and recovery under CMDH and CSDH

To assess the robustness of our findings, we conducted sensitivity analyses across multiple GPP products, climate regimes, vegetation types, event intensities, and event categories.

We first evaluated consistency using four independent GPP datasets (MODIS-GPP, VOD-GPP, GOSIF-GPP, and NIRv-GPP). Daily MODIS-GPP

followed the same framework as BEPS-GPP, whereas the remaining datasets were aggregated to a monthly scale. For these monthly datasets, thresholds and event identification were adjusted accordingly, utilizing a one-month temporal separation limit for event merging. Recovery time at this scale was defined as the number of months required for GPP anomalies to remain above the threshold for at least three consecutive months.

We further examined spatial heterogeneity across climate zones, aridity gradients, and vegetation types to evaluate how the relative dominance of soil- versus atmosphere-driven stress varies geographically. Here the aridity gradient was defined using the aridity index (AI), including extremely arid (AI < 0.03), arid (0.03-0.20), semi-arid (0.20-0.50), semi-humid (0.50-0.65), and humid (> 0.65) conditions. Vegetation types, derived from land cover classifications, were classified into needleleaf forests, broadleaf forests, mixed forests, shrublands, savannas, grasslands, and croplands. To isolate the compound effects of dry-hot extremes, GPP responses under CMDH and CSDH were compared against those from isolated meteorological droughts, soil droughts, and heatwaves. In addition, we also assessed sensitivity of GPP responses to event intensity by classifying compound dry-hot events into moderate, heavy, and extreme levels.

To further characterize the likelihood of GPP losses under varying compound dry-hot conditions, we employed a multivariate copula framework. We constructed trivariate copulas linking GPP loss, T_{max}, and VPD/soil moisture at each grid cell. Marginal distributions for each variable were first fitted using empirical cumulative distribution functions. The joint dependence structure was then modeled using a Gaussian copula. Although alternative copula families (e.g., Clayton, Gumbel, Frank, Student's t) can capture asymmetric or tail-dependent relationships, the Gaussian copula provides a parsimonious and computationally efficient representation suitable for large-scale spatial analysis.[43-45] For each fitted copula, we computed conditional probabilities of GPP loss exceeding specified percentile thresholds (i.e., 30th, 20th, 10th, and 5th percentiles, corresponding to increasingly severe productivity reductions) given compound dry-hot conditions of varying intensity (i.e., moderate, heavy, extreme) as follows (taking VPD as an example):

$$\begin{aligned} &F_{GPP|VPD,T_{max}}(GPP \le gpp | VPD \ge vpd, T_{max} \ge t_{max}) \\ &= \frac{F(GPP \le gpp, VPD \ge vpd, T_{max} \ge t_{max})}{F(VPD \ge vpd, T_{max} \ge t_{max})} \\ &= \frac{F(vpd, gpp) - F(vpd, t_{max}, gpp)}{F(vpd) - F(vpd, t_{max})} \end{aligned} \quad (2)$$

Differences in these conditional probabilities between CMDH and CSDH quantified the extent to which soil moisture deficits, relative to atmospheric dryness, elevate the risk of extreme productivity suppression under concurrent heat stress.

Attribution of GPP responses to CMDH and CSDH

To attribute the drivers of GPP responses under CMDH and CSDH, we applied a combined structural equation modeling (SEM) and explainable machine-learning framework. This was designed to quantify both direct and indirect influences of key environmental variables on GPP loss. SEM were constructed with event-scale GPP loss as the response variable and T_{max}, VPD, precipitation (Precp), soil moisture (SSM), surface shortwave radiation (SSRD), and atmospheric CO_2 concentration as explanatory variables. Prior to analysis, all variables were aggregated at the event scale, standard-normalized (z-score), and linearly detrended to isolate event-scale variability from long-term background changes.[27] Separate models were fitted for CMDH and CSDH events to compare pathway structures, with path coefficients estimated via maximum likelihood methods.

To complement the SEM-based attribution and capture nonlinear relationships among variables, Light Gradient Boosting Machine (LightGBM) models were trained separately for CMDH and CSDH events using the same predictors. Model training employed cross-validation to reduce overfitting and ensure generalization. Following model optimization, Shapley Additive Explanations (SHAP) were computed to quantify the contribution of each predictor to GPP loss. SHAP values were calculated for all samples and aggregated to derive global measures of variable importance. Potential multicollinearity among predictors was further assessed (Table S2), and results indicate generally low collinearity, suggesting limited influence on model performance and SHAP-based interpretation.

RESULTS

Global patterns and differential impacts of CMDH and CSDH on GPP

From 1980 to 2020, both CMDH and CSDH events show widespread increases in frequency across global land regions, with the strongest trends in tropical and subtropical ecosystems and weaker or more heterogeneous changes at higher latitudes (Figure S6). We then examine the global patterns of vegetation responses to CMDH and CSDH events. The global distributions reveal pronounced differences in vegetation sensitivity to CMDH and CSDH (Figure 1). CMDH induces substantial GPP reductions across most vegetated regions (Figure 1A), with pronounced losses in mid-latitude semiarid zones and monsoon-temperate transition regions. The latitudinal profile shows a symmetric amplification of CMDH-induced GPP loss around 30-50°N, where atmospheric dryness dominates plant stress. CSDH exhibits broadly similar spatial patterns (Figure 1C) but leads to stronger GPP reductions. The probability density distributions confirm this shift, with a spatially aggregated mean difference (CSDH minus CMDH) of -1.115 $g{\cdot}C{\cdot}m^{-2}{\cdot}day^{-1}$ (Figure 1E), indicating that soil moisture deficits impose a stronger constraint on photosynthesis than atmospheric dryness. Recovery time shows a complementary pattern. Under CMDH, GPP typically recovers within 6-14 days (Figure 1B), whereas CSDH prolongs recovery by an additional 1-10 days, particularly in water-limited regions (Figure 1D). The mean difference reaches 2.238 days (Figure 1F), highlighting the role of soil moisture legacies in delaying post-stress recovery. Together, these results suggest that atmospheric dryness drives rapid physiological stress, while soil moisture deficits enhance ecosystem memory and slow functional recovery.[46-48]

Long-term changes further reveal a widening divergence between the two event types. Over the past four decades, the difference in GPP loss between two event types shows a significant downward trend (slope = -0.003 $g{\cdot}C{\cdot}m^{-2}{\cdot}day^{-1}{\cdot}yr^{-1}$, $p < 0.05$; Figure 1G), suggesting an intensification of CSDH-induced suppression relative to CMDH. Conversely, recovery time differences increase over time (slope = 0.006 $days{\cdot}yr^{-1}$, $p < 0.05$; Figure 1H), indicating growing persistence of soil moisture limitation. Bivariate response surfaces show that GPP loss intensifies under high temperature combined with high VPD or low soil moisture, with a steeper gradient along the soil moisture dimension (Figures 1I-J).

Building on the global patterns, regional aggregation across the IPCC-AR6 domains further underscores the systematic contrast between CMDH and CSDH impacts. While CMDH generally induces moderate GPP loss and recovery durations (Figures S7B-C), CSDH responses are consistently stronger (Figures S7D-E), especially in dryland regions such as WCA, SAM, and SSA. Although the magnitude varies geographically, the spatial coherence of stronger CSDH effects highlights the pervasive influence of root-zone water limitation across climatic gradients.[49,50] In addition, the temporal evolution of these responses reveals a clearer divergence in ecosystem patterns under CMDH versus CSDH conditions. The CMDH-driven GPP loss trend shows a slight mean decline of -0.0051 $g{\cdot}C{\cdot}m^{-2}{\cdot}day^{-1}{\cdot}yr^{-1}$ globally (Figure S8A). In contrast, CSDH-driven losses exhibit a more negative mean trend (-0.0239 $g{\cdot}C{\cdot}m^{-2}{\cdot}day^{-1}{\cdot}yr^{-1}$; Figure S8C), indicating an accelerating suppression of photosynthesis under compound soil drought and heat. Recovery time exhibits similar patterns, with modest increases under CMDH (mean = 0.0806 $days{\cdot}yr^{-1}$; Figure S8B) but substantially stronger increases under CSDH (mean = 0.1512 $days{\cdot}yr^{-1}$; Figure S8D), demonstrating that recovery from CSDH events is becoming slower and more persistent across the globe. These divergent trends underscore the strengthening role of soil moisture in regulating both the magnitude and persistence of ecosystem responses to compound extremes.[51]

Across multiple GPP observational and remote-sensing products, the contrast between CMDH and CSDH appears with high consistency. MODIS-GPP, NIRv-GPP, GOSIF-GPP, and VOD-GPP consistently show that large regions fall within the regime where CSDH causes greater GPP loss and longer recovery than CMDH (Figure 2), while the opposite pattern occupies a much smaller area. Globally, such regions account for approximately one third to one half of vegetated lands (51.6%, 39.4%, 38.0%, and 44.8% across the four products). Despite methodological and sensor-related differences

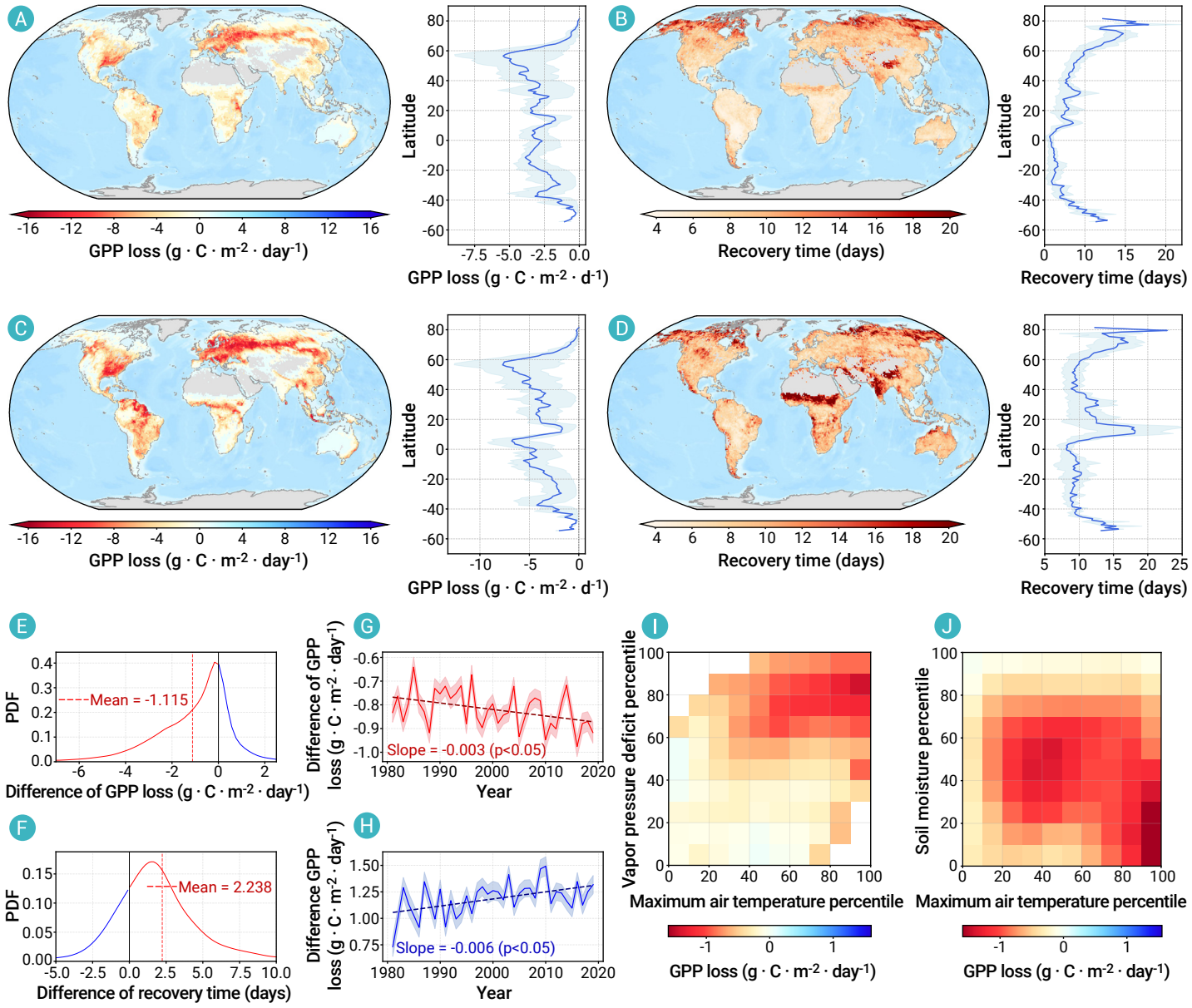

Figure 1. Distributions and differences of GPP loss and recovery time under CMDH and CSDH (A & B) and (C & D) show the distributions of GPP loss and recovery time under CMDH and CSDH, respectively. The right line chart for each panel shows the latitudinal patterns of the GPP loss and recovery time with blue shading indicating the interquartile range (25th-75th percentile). (E) and (F) exhibit the probability density distributions of differences in GPP loss and recovery time between CSDH and CMDH. The red dash line represents the mean difference. (G) and (H) show the temporal variations of differences in GPP loss and recovery time between CSDH and CMDH. The red and blue dashed lines represent the linear regression lines. (I) and (J) show the distributions of CMDH- and CSDH-induced GPP loss under different percentiles of VPD/soil moisture and maximum temperature.

among the products, their agreement points to a robust signal that soil moisture depletion alters the magnitude and persistence of ecosystem stress during compound hot events.[52] Temporal trends across all four GPP products further support this pattern. Differences in recovery time consistently increase over recent decades, whereas differences in GPP loss show a downward trend, indicating strengthening CSDH impacts. Although the GOSIF-GPP trend is weaker and not statistically significant, its direction aligns with the overall pattern. The detailed distributions of GPP loss and recovery time under CMDH and CSDH for the four GPP products can refer to Figures S9-S12. In general, the coherence across diverse data sources strengthens confidence in the global-scale patterns documented above and underscores the central role of soil moisture dynamics in shaping ecosystem responses to compound hot extremes in a warming world.

Spatio-temporal heterogeneity in ecosystem responses to CMDH and CSDH

Figure 3 presents the distributions of CMDH- and CSDH-induced GPP loss and recovery time across five climate zones. Under CMDH, GPP losses are largest in temperate, while polar zones exhibit weaker reductions (Figure 3A). When soil moisture deficits co-occur with heat, GPP losses increase across all climate zones, with the most pronounced amplification in temperate and arid regions (Figure 3B). This amplification reflects the coupling of high evaporative demand with shallow soil water reserves in these regions.[53] Unlike tropical systems where deep rooting and frequent rainfall replenish soil moisture, temperate and arid ecosystems rely on limited water storage that becomes critically depleted when atmospheric demand intensifies during heat extremes, thereby shifting the primary constraint from atmospheric to belowground processes.[54] In tropical systems, although losses deepen under CSDH, their magnitude remains comparatively moderate, consistent with generally higher baseline moisture availability.[55] Recovery time shows distinct patterns across climate zones. Under CMDH, tropical and temperate ecosystems recover rapidly, whereas polar and cold regions exhibit broader distributions and longer recovery tails (Figure 3C). CSDH shifts recovery distributions toward longer durations across all zones, increasing both the mean and vari-

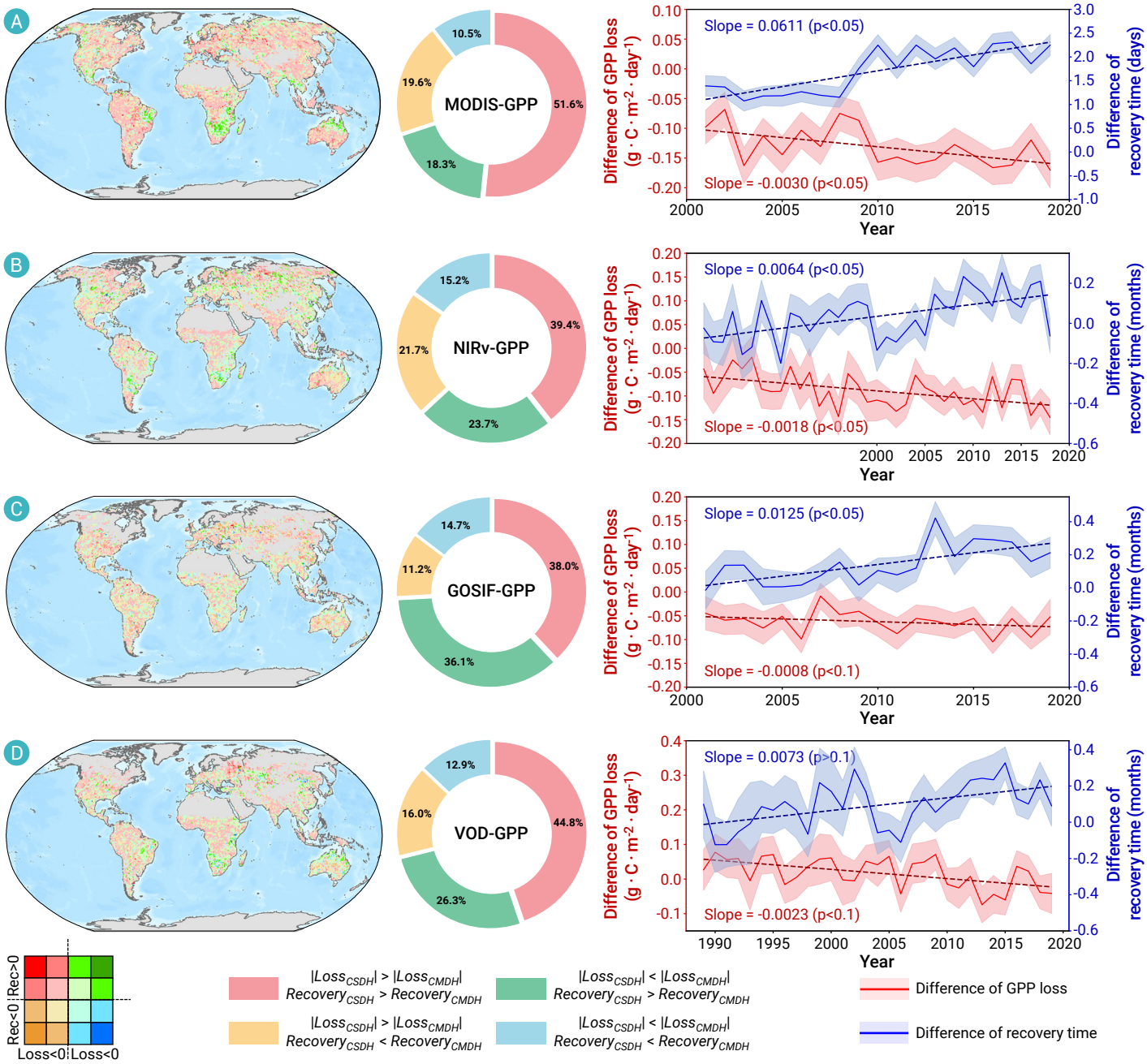

Figure 2. Spatio-temporal heterogeneity in GPP responses to CMDH and CSDH across multiple GPP products (A-D) show the global distributions of CSDH-CMDH differences in GPP loss and recovery time based on MODIS-GPP, NIRv-GPP, GOSIF-GPP, and VOD-GPP, respectively. Red regions indicate stronger and longer-lasting impacts under CSDH, whereas blue regions indicate CMDH dominance. The pie charts summarize the global fractions of each response quadrant. The right panels show temporal variations in differences in GPP loss (red) and recovery time (blue), with solid lines representing multi-year means and shaded areas indicating interquartile ranges. Linear regression slopes are also shown for each product.

ability (Figure 3D). In polar regions, recovery times are consistently long under both CMDH and CSDH, reflecting strong constraints imposed by short growing seasons, low temperatures and delayed soil thaw, which limit the window for physiological recovery even when meteorological conditions improve.

The temporal evolution of CMDH-CSDH differences shows that these climate contrasts have intensified unevenly over the past four decades. For all climate regions, the difference in GPP loss shows significantly downward trend, indicating that CSDH-related productivity suppression has strengthened relative to CMDH persistently (Figures 3E-I). This trend suggests that CSDH-related productivity suppression has strengthened relative to CMDH, likely driven by progressive soil moisture depletion under warming-enhanced evapotranspiration. Recovery time exhibits more differential patterns among five climate zones. The difference in recovery time increases significantly in tropical and temperate regions, but the gap is narrowing in cold and polar regions (Figures 3H-J). In these high-latitude areas, while recovery from both event types remains strongly constrained by low temperatures and short growing seasons, recent warming has disproportionately alleviated temperature limitations on photosynthetic recovery. The extension of growing seasons and earlier phenological onset have effectively reduced the recovery time from CMDH events, which are primarily limited by atmospheric conditions that normalize quickly post-event.[56-58] In contrast, CSDH recovery still requires soil moisture recharge, a process governed by slower hydrological cycles that warming cannot directly accelerate.[59,60] The narrowing gap thus reflects asymmetric warming benefits rather than equivalent recovery capacity under both pathways. Across climate zones, these patterns show that the dominance of CSDH over CMDH emerges most clearly where soil water availability governs both the magnitude of productivity loss and the pace of recovery.

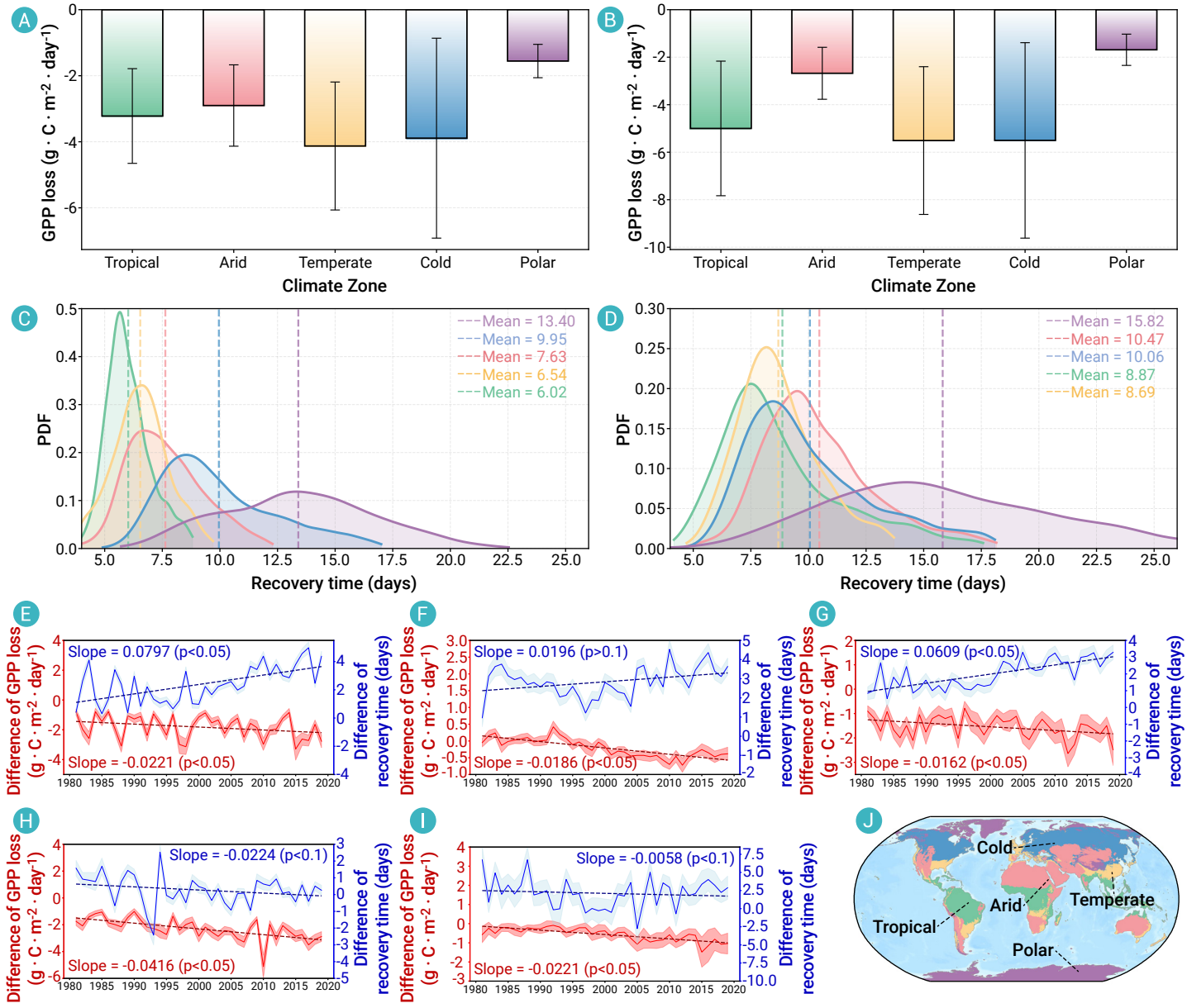

Figure 3. Distributions and long-term trends of CMDH- and CSDH-induced GPP loss and recovery time across five Köppen-Geiger climate zones (A) and (B) show the distributions of mean GPP loss under CMDH and CSDH across five climate zone, respectively. (C) and (D) present probability density distributions of recovery time under CMDH and CSDH, with dashed lines indicating mean values. (E-I) illustrate temporal trends in differences between CSDH and CMDH for GPP loss and recovery time across tropical, arid, temperate, cold, and polar regions. Blue and red lines denote recovery time and GPP loss differences, respectively, with shaded areas indicating interannual variability. (J) shows the global distribution of climate zones.

We further examine the differences along the aridity gradient. GPP losses deepen from extremely arid to semi-humid regions under both CMDH and CSDH, with mean losses increasing from less than -1 g·C·m^{-2}·day^{-1} in extremely arid zones to below -4 g·C·m^{-2}·day^{-1} in humid regions (Figures S13A & C). Recovery times show an opposite spatial ordering. Under CSDH, recovery exceeds 12 days in extremely arid regions and shortens toward humid climates, where mean recovery remains below 9 days (Figures S13B & D). This inverse relationship between loss magnitude and recovery duration reveals contrasting limitation regimes across the aridity gradient. In humid regions, abundant baseline productivity translates to larger absolute GPP losses when stress occurs, yet rapid soil moisture recharge via regular precipitation enables swift recovery. Conversely, arid ecosystems exhibit smaller absolute losses due to inherently low productivity, but recovery is protracted by infrequent rainfall and deep-water deficits that persist long after atmospheric conditions normalize.[61] This pattern underscores a fundamental trade-off that ecosystems adapted to reliable moisture lose more during stress but recover faster, while water-limited systems show modest immediate impacts yet prolonged legacy effects.[62] In general, the resulting heterogeneity reflects not only differences in exposure to compound extremes but also contrasts in ecosystem water and energy constraints under ongoing climate warming.

Following the climate-zone heterogeneity, ecosystem responses also display pronounced differences across vegetation types. Under both CMDH and CSDH, forests experience deeper GPP losses than shrublands and grasslands, with mixed and needleleaf forests showing the most negative mean values (Figures S14A-B). Under CSDH, losses intensify across all vegetation types, but the relative amplification is strongest in woody ecosystems. Grasslands and croplands exhibit smaller absolute losses, although their distributions broaden. Such pattern reveals increased spatial variability in productivity responses when soil moisture deficits accompany heat stress, likely reflecting heterogeneity in rooting depth, soil texture, and management practices that modulate water access under compound stress. Recovery dynamics further differentiate vegetation functional types. Under CMDH, grasslands and croplands recover relatively rapidly, with mean recovery times clustered around 6-8 days, whereas forested ecosystems show longer recovery tails extending beyond 15 days (Figure S14C). CSDH shifts recovery

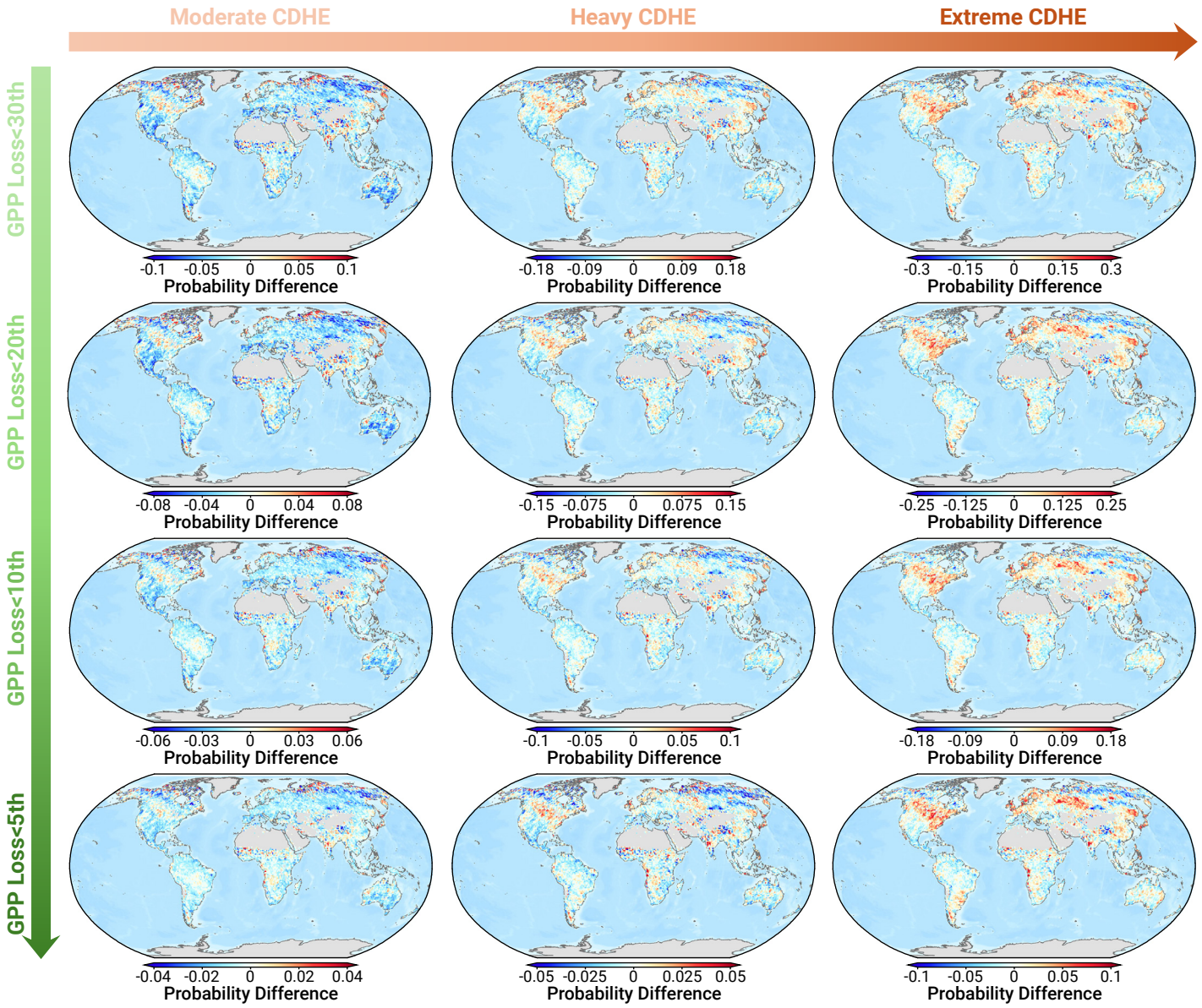

Figure 4. Spatial patterns of probability differences in GPP loss between CSDH and CMDH across increasing compound dry-hot event severity Columns correspond to moderate, heavy, and extreme compound dry-hot events, respectively. Rows show probability differences for GPP loss exceeding the 30th, 20th, 10th, and 5th percentile thresholds. Positive values indicate higher probabilities under CSDH relative to CMDH, whereas negative values indicate CMDH dominance.

distributions toward longer durations for all vegetation types, increasing mean recovery times by approximately 0.5-2 days depending on ecosystem type (Figure S14D). This extension is most evident in needleleaf and mixed forests, where recovery remains consistently slower than in non-woody systems.

Beyond the average impacts, GPP responses also show strong sensitivity to the severity of compound dry-hot events. As event intensity increases from moderate to extreme, both CMDH and CSDH produce larger GPP losses and longer recovery times, with spatial hotspots expanding across mid-latitude and monsoon-temperate transition regions (Figure S15). Under CMDH, moderate events mainly affect semiarid and continental interiors, whereas heavy and extreme events generate widespread losses across Eurasia and North America. CSDH exhibits similar spatial expansion but consistently stronger magnitudes, particularly under heavy and extreme conditions, accompanied by pronounced prolongation of recovery time across most vegetated regions. The probabilistic analysis further reveals a transition in the dominant pathway governing GPP loss as compound dry-hot events intensify (Figure 4). Under moderate events, negative probability differences prevail across large portions of the globe, indicating that CMDH more frequently leads to mild GPP losses than CSDH. As event severity intensifies, areas with positive probability differences expand. Under heavy events, CSDH shows elevated probabilities for both moderate and severe GPP losses, while CMDH dominates only in limited regions and primarily at lower loss levels. For extreme compound dry-hot events, the probabilistic divergence becomes most pronounced. CSDH increases the likelihood of large GPP losses exceeding the 20th, 10th and especially the 5th percentile thresholds, with coherent hotspots spanning mid-latitude Eurasia, central North America and parts of South America. In contrast, CMDH-related probabilities remain comparatively concentrated at lower loss levels. This distribution difference may be explained that atmospheric dryness primarily regulates short-term stomatal closure, limiting productivity but providing protection against catastrophic tissue damage.[63,64] Soil moisture deficits, however, can trigger cascading hydraulic failure when severe, leading to canopy dieback and prolonged suppression that generates extreme GPP losses.[65] Such shift toward higher loss under CSDH demonstrates that soil moisture deficits play a more important role in governing the upper extremes of ecosystem carbon loss. This progression from CMDH dominance under moderate conditions to CSDH dominance under extreme conditions highlights a nonlinear transition in ecosystem vulnerability. At lower stress levels, vegetation responses are primarily controlled by atmospheric demand, whereas at higher intensities,

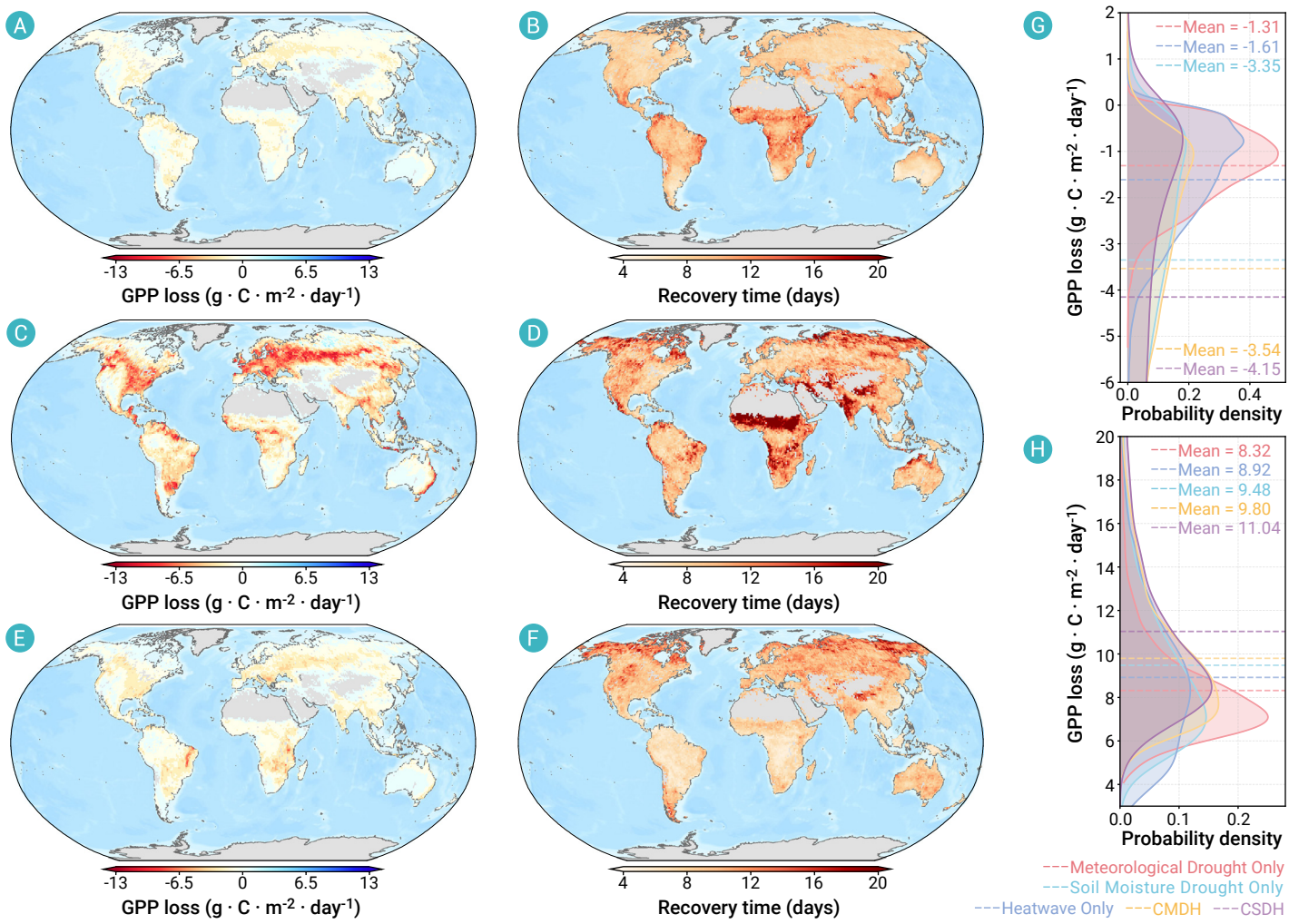

Figure 5. Comparison between compound and individual extremes (A) and (B) show the spatial distributions of GPP loss and recovery time under meteorological drought only, (C) and (D) show the corresponding patterns under soil moisture drought only, and (E) and (F) show those under heatwave only. (G) and (H) show the probability density distributions comparing individual extremes with CMDH and CSDH.

soil moisture deficit becomes the critical factor shaping the upper tail of the loss distribution. This probabilistic perspective underscores that soil moisture constraints increasingly dominate ecosystem vulnerability as compound dry-hot events intensify, shaping both the frequency and severity of extreme GPP reductions.

To disentangle the role of compound events on GPP, we further compare vegetation responses under isolated meteorological drought, soil moisture drought, and heatwave conditions. Individually, meteorological drought produces moderate GPP reductions with relatively short recovery times, while soil moisture drought and heatwave generate stronger losses and longer recovery across most regions (Figures 5A-F). The probability density distributions also highlight differences between isolated and compound extremes. Isolated events cluster toward weaker GPP losses and shorter recovery, whereas compound events shift both distributions toward heavier losses and prolonged recovery (Figures 5G-H). CMDH intensifies GPP loss relative to single heat or drought events, but CSDH exhibits the strongest shift in loss distributions and the longest recovery tails, with mean recovery exceeding 10 days. These patterns demonstrate that the co-occurrence of heatwave with soil moisture deficits significantly alters both the magnitude and persistence of ecosystem stress, producing impacts that cannot be inferred from isolated extremes alone.

Drivers and future changes in GPP loss and recovery under CMDH and CSDH

Building on the contrasting GPP responses, we further investigate the mechanistic pathways regulating GPP loss under CMDH and CSDH using SEM and SHAP analyses (Figure 6). Under CMDH, GPP loss is dominated by atmospheric demand-driven pathways. Maximum temperature (coefficient = -0.193, $p < 0.001$) and VPD (-0.245, $p < 0.001$) exert strong direct constraints, with temperature further amplifying VPD (0.681, $p < 0.001$). This pathway reflects rapid, reversible stomatal regulation under high atmospheric demand, explaining why productivity losses are acute but short-lived[11]. Incoming shortwave radiation mainly acts upstream by amplifying both maximum temperature (0.396, $p < 0.001$) and VPD (0.177, $p < 0.001$), whereas its direct pathway to GPP loss remains relatively weak (-0.077, $p < 0.001$). Soil moisture plays a secondary role in this pathway, contributing modestly to loss amplification (0.161, $p < 0.001$) and largely reflecting concurrent precipitation variability. Consistently, SHAP results indicate that temperature and VPD (23.8% and 21.3%, respectively) together explain over half of the variance in CMDH-induced GPP loss.

In contrast, CSDH exhibits a clear shift toward soil moisture control. Although temperature remains influential (-0.218, $p < 0.001$), its effects increasingly propagate through soil water depletion, as indicated by a strong negative linkage between maximum temperature and soil moisture. Soil moisture emerges as the dominant driver (0.283, $p < 0.001$), exceeding atmospheric contributions, while the relative importance of VPD declines (-0.182, $p < 0.001$). Under CSDH, the constraint transitions from rapid, reversible stomatal closure to prolonged hydraulic stress. When soil moisture depletes below critical thresholds, plants cannot maintain sufficient water potential gradients to support photosynthesis, even if atmospheric conditions improve.[66] Unlike stomatal responses that reverse within hours to days, soil moisture recovery requires hydrological recharge through precipitation events, creating

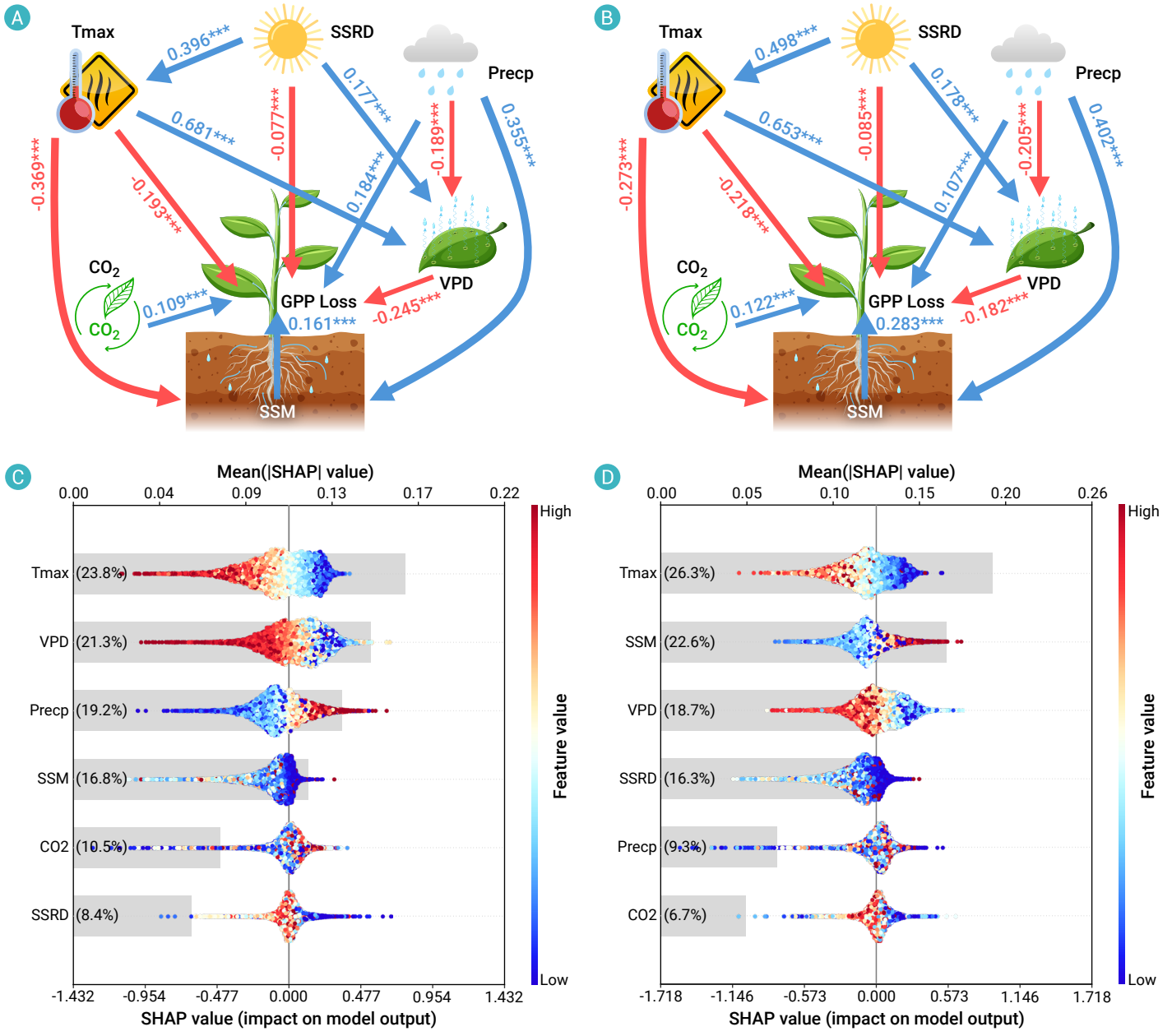

Figure 6. Attribution of CMDH- and CSDH-induced GPP loss based on SEM and SHAP analyses (A) and (B) show SEM path diagrams for CMDH and CSDH, respectively, with arrows indicating standardized path coefficients (red for negative effects and blue for positive effects). (C) and (D) present SHAP summary plots for CMDH and CSDH, showing the relative contributions of T_{max}, VPD, soil moisture (SSM), precipitation (Precp), surface shortwave radiation (SSRD), and CO_2 to GPP loss. Points are colored by feature value, illustrating how variable states modulate their contributions to productivity suppression.

persistent ecosystem memory that extends far beyond the meteorological duration of the compound event.[64,67] Moreover, soil physical properties further modulate this pathway. Regions dominated by sandy soils tend to experience amplified GPP loss and prolonged recovery due to their low water-holding capacity and rapid moisture depletion, whereas clay soils can partially buffer short-term deficits and facilitate more stable post-event recovery (Figure S16). These patterns are further supported by SHAP-based contribution, in which soil moisture emerges as a co-dominant contributor under CSDH (22.6%). Precipitation assumes a more indirect role under CSDH through its control on SSM (0.402, $p < 0.001$), highlighting the importance of hydrological recharge in constraining loss severity once soil moisture becomes the primary constraint. CO_2 shows a small but consistently positive contribution in both pathways, suggesting partial buffering that remains insufficient to counteract compound stress.

Future projections indicate a systematic intensification of these differences under climate change (Figure 7). Across SSP scenarios, both CMDH- and CSDH-induced GPP losses increase from the near to far future, but CSDH consistently produces larger losses and broader spatial variability. This divergence reflects increasing heterogeneity in soil moisture sensitivity, with ecosystems becoming more strongly regulated by regional hydrological conditions rather than atmospheric forcing alone. This divergence is further clarified by the temporal evolution of the CSDH-CMDH difference across SSP scenarios (Figures 7E-F). For GPP loss, the differences show downward trends in all scenarios, with the strongest negative slopes emerging under SSP3-7.0 (slope = -0.0059 $g{\cdot}C{\cdot}m^{-2}{\cdot}month^{-1}{\cdot}yr^{-1}$, $p < 0.1$) and SSP5-8.5 (slope=-0.0295 $g{\cdot}C{\cdot}m^{-2}{\cdot}month^{-1}{\cdot}yr^{-1}$, $p < 0.05$). The acceleration of CSDH dominance under high-forcing scenarios reflects multiple reinforcing processes: (1) enhanced evapotranspiration under warming depletes soil moisture faster, (2) more frequent and intense heat extremes exhaust shallow soil water reserves before precipitation can replenish them, and (3) shifts in precipitation seasonality create longer dry periods between recharge events.[68,69] These mechanisms progressively shift ecosystems from atmospheric- to soil-limited regimes, amplifying the sensitivity to soil moisture deficits.

Under SSP2-4.5 and SSP5-8.5 scenarios, Spatially, regions where CSDH

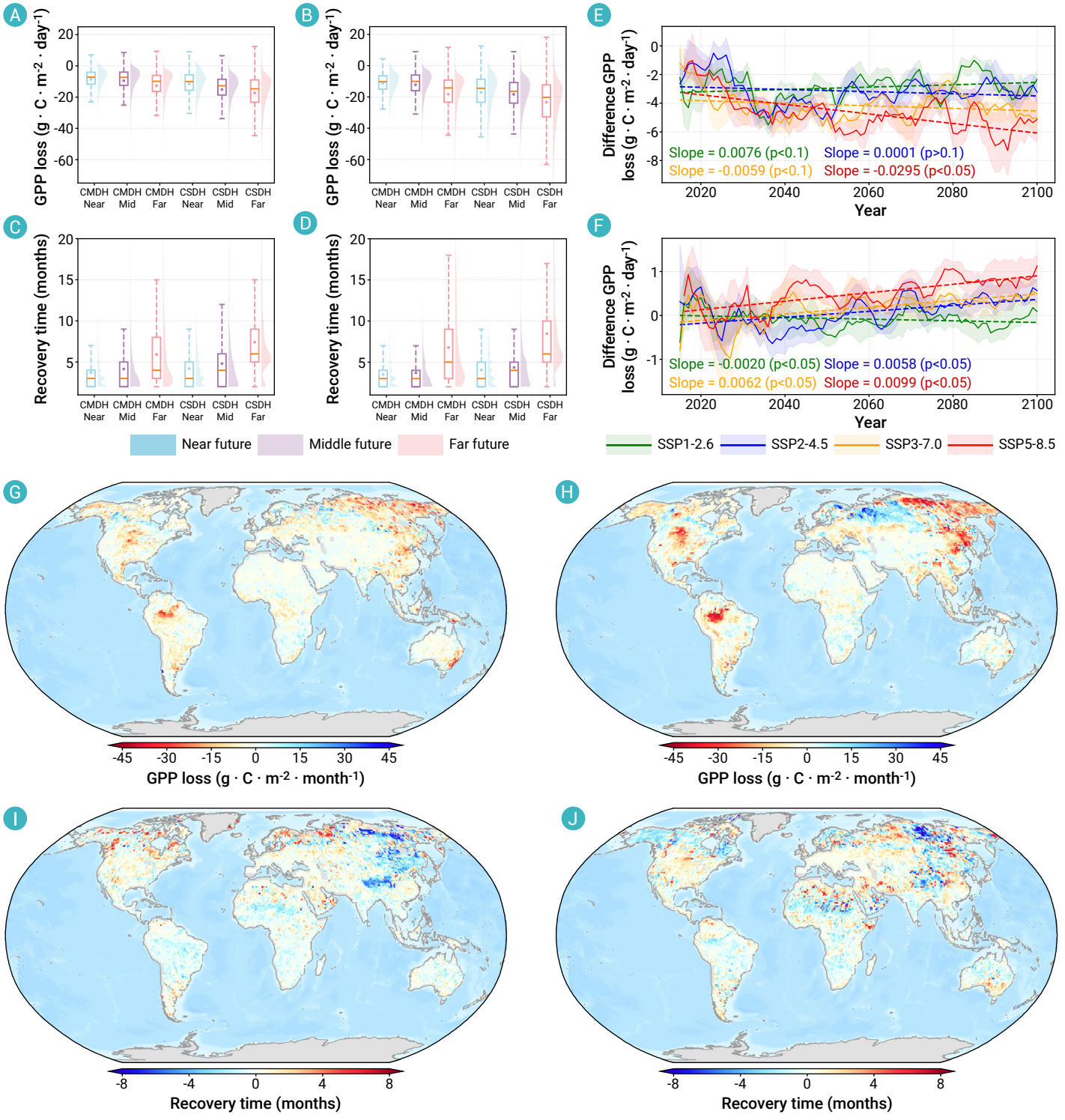

Figure 7. Projected changes in GPP loss and recovery under CMDH and CSDH across future climate scenarios (A-D) show distributions of GPP loss and recovery time under near-, mid-, and far-future periods for CMDH and CSDH. (E) and (F) illustrate temporal evolutions of differences between CSDH and CMDH in GPP loss and recovery time, with colored lines representing different SSP scenarios and shaded areas indicating interannual variability. (G-J) show spatial distributions of future differences in GPP loss and recovery time under SSP2-4.5 and SSP5-8.5 scenarios.

dominates expand across mid- to high-latitude Eurasia, central North America, and parts of South America, consistent with projected drying and increased evaporative demand. (Figures 7G-H). While the magnitude of the trends varies among scenarios, their consistent direction suggests that warming-induced soil moisture limitation increasingly amplifies productivity losses beyond what can be explained by atmospheric demand with heatwave. In contrast, the difference in recovery time shows a prominent upward trend across all SSPs, with the slopes achieving 0.0062 months·yr^{-1} ($p < 0.05$) and 0.0099 months·yr^{-1} ($p < 0.05$) under SSP3-7.0 and SSP5-8.5 scenarios, respectively. The spatial distributions of recovery time differences also exhibit certain heterogeneity, with large portions of the Northern Hemisphere showing prolonged recovery under CSDH, particularly under SSP585 (Figures 7I-J). This pattern suggests that future ecosystems will not only experience deeper carbon losses during compound soil dry-hot events but will also require longer periods to regain pre-event productivity levels. The supplementary maps of GPP loss and recovery time under four SSPs (Figures S17-S18)

provide additional context for these differences. Although both CMDH and CSDH impacts intensify with increasing radiative forcing, CSDH shows a more pronounced amplification in both loss severity and recovery duration, particularly under SSP370 and SSP585. Regions already identified as CSDH-sensitive in the historical period remain persistent hotspots in future projections, suggesting that background aridification and soil moisture memory progressively shape ecosystem responses to compound heat stress.

DISCUSSION

The increasing concurrence of drought and heat is a defining feature of contemporary climate extremes, yet ecosystem responses have largely been interpreted through atmospheric conditions alone. By distinguishing compound meteorological dry-hot from compound soil dry-hot events, we reveal a systematic divergence in both the magnitude and persistence of productivity responses. Across regions, ecosystems, and scenarios, CSDH consistently induces larger GPP losses and longer recovery times, highlighting the growing dominance of subsurface water limitation under a warming climate.

This divergence reflects distinct but interacting stress pathways. CMDH imposes rapid atmospheric constraints via elevated temperature and VPD, leading to immediate but transient suppression of photosynthesis.[70] In contrast, CSDH couples thermal stress with depleted soil moisture, extending water limitation beyond the relaxation of atmospheric anomalies.[17,27] This results in amplified GPP reductions and prolonged recovery, indicating stronger ecosystem memory under soil-coupled extremes, particularly in water-limited environments.

Pronounced spatial heterogeneity further clarify the climatic controls of these processes. In tropical and temperate regions, the recovery gap between CSDH and CMDH has widened over recent decades, consistent with increasing evaporative demand and reduced soil moisture recharge. High-productivity ecosystems with shallow rooting systems in these regions are especially sensitive to post-event water availability. By contrast, cold and polar regions show a narrowing gap, likely due to warming-induced alleviation of thermal constraints, increased snowmelt contributions, and a reduced role of atmospheric drought.[71-73] In such regions, warming may partially offset soil moisture deficits by alleviating thermal limitations, dampening the contrast between meteorological and soil-coupled extremes.

Previous studies have emphasized compound drought–heat impacts primarily from an atmospheric perspective, documenting substantial GPP losses followed by relatively rapid recovery.[9,74-76] This body of work has been essential in establishing the global prevalence of compound extremes and in demonstrating their amplified effects on vegetation carbon uptake. Our results reconcile these findings by showing that recovery dynamics critically depend on soil moisture conditions. By distinguishing soil-coupled from atmosphere-driven compound extremes, we find that similar atmospheric anomalies can produce markedly different post-event patterns. Where soil moisture deficits persist, recovery is delayed even after atmospheric conditions normalize, and repeated events can accumulate legacy effects, progressively strengthening hydrological constraints. From this perspective, differences among previous studies regarding ecosystem resilience to drought-heat extremes can be understood as reflecting variations in underlying soil moisture states rather than inconsistencies in ecosystem response.

The mechanistic basis of this divergence is further supported by the combined SEM and SHAP analyses. Under CMDH, GPP loss is predominantly mediated by temperature and VPD pathways, reflecting rapid atmospheric control. Under CSDH, soil moisture emerges as the primary constraint on productivity, exerting both direct suppression of carbon uptake and indirect modulation of atmospheric stress sensitivity. This is consistent with previous findings that recovery processes are strongly governed by hydrological conditions and bioclimatic context, with soil moisture availability playing a dominant role in determining both the magnitude and persistence of vegetation responses.[46,77] Quantitatively, stronger soil moisture-GPP linkages and enhanced indirect effects via precipitation and VPD highlight a reorganization of control pathways under soil-coupled extremes. These mechanisms explain why CSDH-related impacts are not only larger in magnitude but also persist longer, even after atmospheric anomalies subside.

Several limitations in this study should also be acknowledged. Soil moisture estimates are derived from model-assimilated datasets and may underrepresent deep soil and groundwater contributions, although sensitivity analyses using root-zone and detrended soil moisture support the robustness of our conclusions (Text S1- S2 & Figures S19-S20).[78] Second, the analysis focuses on short- to medium-term productivity responses and does not explicitly account for structural vegetation changes, such as mortality, compositional shifts, or biome transitions, which may occur under repeated or extreme compound events and further alter long-term carbon dynamics.[79] Furthermore, a uniform temporal threshold was adopted to define ecosystem recovery across all vegetation types in this study. While vegetation phenology may influence recovery dynamics, defining optimal, vegetation-specific thresholds at the global scale remains challenging due to strong interactions among vegetation type, climate conditions, and event characteristics.

Despite these uncertainties, the results have clear implications for understanding ecosystem risk under climate change. As warming progresses, compound dry-hot impacts on terrestrial productivity will increasingly be mediated by soil moisture dynamics rather than atmospheric anomalies alone. Incorporating soil-coupled extremes, recovery processes, and event severity into assessments of ecosystem resilience provides a more realistic basis for anticipating future changes in terrestrial carbon uptake and for informing adaptation strategies under escalating climate extremes.

REFERENCES

1. Gui Y., Wang K., Huntingford C., et al. (2025). Vegetation greenness in 2024. *Nat. Rev. Earth Environ.* **6**:255–257. DOI:10.1038/s43017-025-00656-z
2. Anav A., Friedlingstein P., Beer C., et al. (2015). Spatiotemporal patterns of terrestrial gross primary production: A review. *Rev. Geophys.* **53**:785–818. DOI:10.1002/2015rg000483
3. Smith T., Traxl D. and Boers N. (2022). Empirical evidence for recent global shifts in vegetation resilience. *Nat. Clim. Change* **12**:477–484. DOI:10.1038/s41558-022-01352-2
4. Beer C., Reichstein M., Tomelleri E., et al. (2010). Terrestrial gross carbon dioxide uptake: Global distribution and covariation with climate. *Science* **329**:834–838. DOI:10.1126/science.1184984
5. Reichstein M., Bahn M., Ciais P., et al. (2013). Climate extremes and the carbon cycle. *Nature* **500**:287–295. DOI:10.1038/nature12350
6. Huang S., Wang S., Wang C., et al. (2025). Differential sensitivities of three types of compound drought and heatwave events to human-induced climate change across the globe. *Weather Clim. Extremes* **50**. DOI:10.1016/j.wace.2025.100836
7. AghaKouchak A., Chiang F., Huning L. S., et al. (2020). Climate extremes and compound hazards in a warming world. *Annu. Rev. Earth Planet. Sci.* **48**:519–548. DOI:10.1146/annurev-earth-071719-055228
8. Bastos A., Ciais P., Friedlingstein P., et al. Direct and seasonal legacy effects of the 2018 heat wave and drought on European ecosystem productivity. *Sci. Adv.* **6**:eaba2724. DOI:10.1126/sciadv.aba2724
9. Yao Y., Fu B., Liu Y., et al. (2024). Compound hot–dry events greatly prolong the recovery time of dryland ecosystems. *Natl. Sci. Rev.* **11**:nwae274. DOI:10.1093/nsr/nwae274
10. Yan W., Zhou J., Wang X., et al. (2025). Vegetation resistance to compound drought and heatwave events buffers the spatial shift velocities of vegetation vulnerability. *Commun. Earth Environ.* **6**:320. DOI:10.1038/s43247-025-02298-x
11. Lin S., Chen X., Xia J., et al. (2025). Global vegetation production may decrease in this century due to rising atmospheric dryness. *Nat. Ecol. Evol.* **9**:2279–2289. DOI:10.1038/s41559-025-02885-3
12. Tripathy K. P., Mukherjee S., Mishra A. K., et al. (2023). Climate change will accelerate the high-end risk of compound drought and heatwave events. *Proc. Natl. Acad. Sci. USA* **120**:e2219825120. DOI:10.1073/pnas.2219825120
13. Zscheischler J., Westra S., van den Hurk B. J. J. M., et al. (2018). Future climate risk from compound events. *Nat. Clim. Change* **8**:469–477. DOI:10.1038/s41558-018-0156-3
14. Zscheischler J., Reichstein M., von Buttlar J., et al. (2014). Carbon cycle extremes during the 21st century in CMIP5 models: Future evolution and attribution to climatic drivers. *Geophys. Res. Lett.* **41**:8853–8861. DOI:10.1002/2014gl062409
15. Zhou S., Williams A. P., Berg A. M., et al. (2019). Land–atmosphere feedbacks exacerbate concurrent soil drought and atmospheric aridity. *Proc. Natl. Acad. Sci. USA* **116**:18848–18853. DOI:10.1073/pnas.1904955116
16. Zhang G., Zhang S., Wang H., et al. (2024). Biodiversity and wetting of climate alleviate vegetation vulnerability under compound drought - hot extremes. *Geophys. Res. Lett.* **51**:e2024GL108396. DOI:10.1029/2024gl108396
17. Li J., Zhang Y., Bevacqua E., et al. (2024). Future increase in compound soil drought-heat extremes exacerbated by vegetation greening. *Nat. Commun.* **15**:10875. DOI:10.1038/s41467-024-55175-0
18. Piao S., Wang X., Park T., et al. (2019). Characteristics, drivers and feedbacks of global greening. *Nat. Rev. Earth Environ.* **1**:14–27. DOI:10.1038/s43017-019-0001-x

19. Seneviratne S., Nicholls N., Easterling D., et al. (2012). Changes in climate extremes and their impacts on the natural physical environment. Field C.B., Barros V., Stocker T.F., Qin D. (eds). Managing the risks of extreme events and disasters to advance climate change adaptation: Special report of the intergovernmental panel on climate change. (Cambridge University Press), pp:109-230. DOI:10.1017/CBO9781139177245.006
20. Seneviratne S. I., Corti T., Davin E. L., et al. (2010). Investigating soil moisture–climate interactions in a changing climate: A review. *Earth-Sci. Rev.* **99**:125–161. DOI:10.1016/j.earscirev.2010.02.004
21. Yuan W., Zheng Y., Piao S., et al. (2019). Increased atmospheric vapor pressure deficit reduces global vegetation growth. *Sci. Adv.* **5**:eaax1396. DOI:10.1126/sciadv.aax1396
22. Lian X., Li Y., Liu J., et al. (2025). Northern ecosystem productivity reduced by Rossby-wave-driven hot–dry conditions. *Nat. Geosci.* **18**:615–623. DOI:10.1038/s41561-025-01722-3
23. Huang M. and Zhai P. (2025). Protracted vegetation recovery after compound drought and hot extreme compared to general drought. *Environ. Res. Lett.* **20**:024001. DOI:10.1088/1748-9326/ada4c3
24. Liu Z., Jiao L. and Lian X. (2025). Changes in compound extreme events and their impacts on cropland productivity in China, 1985–2019. *Earths Future* **13**:e2024EF005038. DOI:10.1029/2024ef005038
25. Wu R., Wang Z., Meng F., et al. (2025). Strengthening coupling between vegetation and soil - atmosphere compound drought over the past two decades. *Earths Future* **13**:e2025EF006311. DOI:10.1029/2025ef006311
26. Hughes T. P., Kerry J. T., Connolly S. R., et al. (2018). Ecological memory modifies the cumulative impact of recurrent climate extremes. *Nat. Clim. Change* **9**:40–43. DOI:10.1038/s41558-018-0351-2
27. Wang T., Zhang J., Li Z., et al. (2025). Roles of soil and atmospheric dryness on terrestrial vegetation productivity in China-which dominates at what thresholds. *Earths Future* **13**:e2024EF005469. DOI:10.1029/2024ef005469
28. Zhao D., Zhang Z. and Zhang Y. (2023). Soil moisture dominates the forest productivity decline during the 2022 China compound drought - heatwave event. *Geophys. Res. Lett.* **50**:e2023GL104539. DOI:10.1029/2023gl104539
29. Zscheischler J., Martius O., Westra S., et al. (2020). A typology of compound weather and climate events. *Nat. Rev. Earth Environ.* **1**:333–347. DOI:10.1038/s43017-020-0060-z
30. Zhou S., Zhang Y., Park Williams A., et al. (2019). Projected increases in intensity, frequency, and terrestrial carbon costs of compound drought and aridity events. *Sci. Adv.* **5**:eaau5740. DOI:10.1126/sciadv.aau5740
31. Byrne M. P. and O'Gorman P. A. (2018). Trends in continental temperature and humidity directly linked to ocean warming. *Proc. Natl. Acad. Sci. USA* **115**:4863–4868. DOI:10.1073/pnas.1722312115
32. Zhou S., Williams A. P., Lintner B. R., et al. (2021). Soil moisture–atmosphere feedbacks mitigate declining water availability in drylands. *Nat. Clim. Change* **11**:38–44. DOI:10.1038/s41558-020-00945-z
33. He Q., Ju W., Dai S., et al. (2021). Drought risk of global terrestrial gross primary productivity over the last 40 years detected by a remote sensing - driven process model. *J. Geophys. Res. Biogeosci.* **126**:e2020JG005944. DOI:10.1029/2020jg005944
34. Joiner, J., and Y. Yoshida. (2021). Global MODIS and FLUXNET-derived daily gross primary production, V2. ORNL DAAC, Oak Ridge, Tennessee, USA. DOI:10.3334/ORNLDAAC/1835.
35. Li X. and Xiao J. (2019). Mapping photosynthesis solely from solar-induced chlorophyll fluorescence: A global, fine-resolution dataset of gross primary production derived from OCO-2. *Remote Sens.* **11**:2563. DOI:10.3390/rs11212563
36. Wild B., Teubner I., Moesinger L., et al. (2022). VODCA2GPP – a new, global, long-term (1988–2020) gross primary production dataset from microwave remote sensing. *Earth Syst. Sci. Data* **14**:1063–1085. DOI:10.5194/essd-14-1063-2022
37. Wang S., Zhang Y., Ju W., et al. (2021). Tracking the seasonal and inter-annual variations of global gross primary production during last four decades using satellite near-infrared reflectance data. *Sci. Total Environ.* **755**:142569. DOI:10.1016/j.scitotenv.2020.142569
38. Muñoz-Sabater J., Dutra E., Agustí-Panareda A., et al. (2021). ERA5-Land: A state-of-the-art global reanalysis dataset for land applications. *Earth Syst. Sci. Data* **13**:4349–4383. DOI:10.5194/essd-13-4349-2021
39. Beck H. E., Zimmermann N. E., McVicar T. R., et al. (2018). Present and future Köppen-Geiger climate classification maps at 1-km resolution. *Sci. Data* **5**:180214. DOI:10.1038/sdata.2018.214
40. Yin J., Gentine P., Slater L., et al. (2023). Future socio-ecosystem productivity threatened by compound drought–heatwave events. *Nat. Sustain.* **6**:259–272. DOI:10.1038/s41893-022-01024-1
41. Zhang X., Hegerl G., Zwiers F. W., et al. (2005). Avoiding inhomogeneity in percentile-based indices of temperature extremes. *J. Clim.* **18**:1641–1651. DOI:10.1175/JCLI3366.1
42. Liu L., Gudmundsson L., Hauser M., et al. (2019). Revisiting assessments of ecosystem drought recovery. *Environ. Res. Lett.* **14**:114028. DOI:10.1088/1748-9326/ab4c61
43. Ben Alaya M. A., Chebana F. and Ouarda T. B. M. J. (2014). Probabilistic gaussian copula regression model for multisite and multivariable downscaling. *J. Clim.* **27**:3331–3347. DOI:10.1175/JCLI-D-13-00333.1
44. Suo N., Xu C., Cao L., et al. (2024). A copula-based parametric composite drought index for drought monitoring and applicability in arid Central Asia. *Catena* **235**:107624. DOI:10.1016/j.catena.2023.107624
45. Zhang G., Zhang S., Wang H., et al. (2024). Evaluating vegetation vulnerability under compound dry and hot conditions using vine copula across global lands. *J. Hydrol.* **631**:130775. DOI:10.1016/j.jhydrol.2024.130775
46. Yao Y., Liu Y., Zhou S., et al. (2023). Soil moisture determines the recovery time of ecosystems from drought. *Global Change Biol.* **29**:3562–3574. DOI:10.1111/gcb.16620
47. Novick K. A., Ficklin D. L., Stoy P. C., et al. (2016). The increasing importance of atmospheric demand for ecosystem water and carbon fluxes. *Nat. Clim. Change* **6**:1023–1027. DOI:10.1038/nclimate3114
48. Kannenberg S. A., Novick K. A., Alexander M. R., et al. (2019). Linking drought legacy effects across scales: From leaves to tree rings to ecosystems. *Global Change Biol.* **25**:2978–2992. DOI:10.1111/gcb.14710
49. Stocker B. D., Tumber-Dávila S. J., Konings A. G., et al. (2023). Global patterns of water storage in the rooting zones of vegetation. *Nat. Geosci.* **16**:250–256. DOI:10.1038/s41561-023-01125-2
50. Stocker B. D., Zscheischler J., Keenan T. F., et al. (2018). Quantifying soil moisture impacts on light use efficiency across biomes. *New Phytol.* **218**:1430–1449. DOI:10.1111/nph.15123
51. Humphrey V., Berg A., Ciais P., et al. (2021). Soil moisture–atmosphere feedback dominates land carbon uptake variability. *Nature* **592**:65–69. DOI:10.1038/s41586-021-03325-5
52. Green J. K., Seneviratne S. I., Berg A. M., et al. (2019). Large influence of soil moisture on long-term terrestrial carbon uptake. *Nature* **565**:476–479. DOI:10.1038/s41586-018-0848-x
53. Massmann A., Gentine P. and Lin C. (2019). When does vapor pressure deficit drive or reduce evapotranspiration. *J. Adv. Model. Earth Syst.* **11**:3305–3320. DOI:10.1029/2019ms001790
54. Collins D. B. G. and Bras R. L. (2007). Plant rooting strategies in water - limited ecosystems. *Water Resour. Res.* **43**:W06407. DOI:10.1029/2006wr005541
55. Fan Y., Miguez-Macho G., Jobbágy E. G., et al. (2017). Hydrologic regulation of plant rooting depth. *Proc. Natl. Acad. Sci. USA* **114**:10572–10577. DOI:10.1073/pnas.1712381114
56. Berner L. T., Beck P. S. A., Bunn A. G., et al. (2013). Plant response to climate change along the forest - tundra ecotone in northeastern Siberia. *Global Change Biol.* **19**:3449–3462. DOI:10.1111/gcb.12304
57. Xu L., Myneni R. B., Chapin Iii F. S., et al. (2013). Temperature and vegetation seasonality diminishment over northern lands. *Nat. Clim. Change* **3**:581–586. DOI:10.1038/nclimate1836
58. Richardson A. D., Keenan T. F., Migliavacca M., et al. (2013). Climate change, phenology, and phenological control of vegetation feedbacks to the climate system. *Agric. For. Meteorol.* **169**:156–173. DOI:10.1016/j.agrformet.2012.09.012
59. Maxwell R. M. and Condon L. E. (2016). Connections between groundwater flow and transpiration partitioning. *Science* **353**:377–380. DOI:10.1126/science.aaf7891
60. Orth R. and Seneviratne S. I. (2012). Analysis of soil moisture memory from observations in Europe. *J. Geophys. Res. Atmos.* **117**:D15115. DOI:10.1029/2011jd017366
61. Han Y., Qu Y., Jiang T., et al. (2025). Ecosystems resilience assessment of forest and grassland subjected to ecological drought. *Ecol. Indic.* **173**:113437. DOI:10.1016/j.ecolind.2025.113437
62. Wilcox K. R., Shi Z., Gherardi L. A., et al. (2017). Asymmetric responses of primary productivity to precipitation extremes: A synthesis of grassland precipitation manipulation experiments. *Global Change Biol.* **23**:4376–4385. DOI:10.1111/gcb.13706
63. Grossiord C., Buckley T. N., Cernusak L. A., et al. (2020). Plant responses to rising vapor pressure deficit. *New Phytol.* **226**:1550–1566. DOI:10.1111/nph.16485
64. McDowell N., Pockman W. T., Allen C. D., et al. (2008). Mechanisms of plant survival and mortality during drought: Why do some plants survive while others succumb to drought. *New Phytol.* **178**:719–739. DOI:10.1111/j.1469-8137.2008.02436.x
65. Anderegg W. R. L., Kane J. M. and Anderegg L. D. L. (2012). Consequences of widespread tree mortality triggered by drought and temperature stress. *Nat. Clim. Change* **3**:30–36. DOI:10.1038/nclimate1635
66. Anderegg W. R. L., Schwalm C., Biondi F., et al. (2015). Pervasive drought legacies in forest ecosystems and their implications for carbon cycle models. *Science* **349**:528–532. DOI:10.1126/science.aab1833
67. Peltier D. M. P. and Ogle K. (2019). Legacies of more frequent drought in ponderosa pine across the western United States. *Global Change Biol.* **25**:3803–3816. DOI:10.1111/gcb.14720
68. Chen Z., Qian Z., Huang B., et al. (2025). Increased drought impacts on vegetation productivity in drylands under climate change. *Geophys. Res. Lett.* **52**:e2025GL115616. DOI:10.1029/2025gl115616
69. Bai Y. H., Chen J., Zhang Y. W., et al. (2025). Response modes of global vegetation to extreme drought. *Global Change Biol.* **31**:e70488. DOI:10.1111/gcb.70488
70. Urban J., Ingwers M., McGuire M. A., et al. (2017). Stomatal conductance increases with rising temperature. *Plant Signaling Behav.* **12**:e1356534. DOI:10.1080/15592324.2017.1356534

71. Keenan T. F., Gray J., Friedl M. A., et al. (2014). Net carbon uptake has increased through warming-induced changes in temperate forest phenology. *Nat. Clim. Change* **4**:598–604. DOI:10.1038/nclimate2253
72. Jeong S.-J., Ho C.-H., Gim H.-J., et al. (2011). Phenology shifts at start vs. end of growing season in temperate vegetation over the Northern Hemisphere for the period 1982-2008. *Global Change Biol.* **17**:2385-2399. DOI:10.1111/j.1365-2486.2011.02397.x
73. Barnett T. P., Adam J. C. and Lettenmaier D. P. (2005). Potential impacts of a warming climate on water availability in snow-dominated regions. *Nature* **438**:303–309. DOI:10.1038/nature04141
74. Shi W., Zhang K., Huang S., et al. (2025). Widespread declining sensitivity of terrestrial gross primary productivity to compound dry-hot extremes in China. *J. Hydrol.* **660**:133387. DOI:10.1016/j.jhydrol.2025.133387
75. Liu Z., Jiao L. and Lian X. (2025). Impacts of increasing compound hot-dry events on vegetation under the warming-wetting trend in Northwest China. *Geogr. Sustain.* **6**:100222. DOI:10.1016/j.geosus.2024.08.003
76. Jiao T., Williams C. A., De Kauwe M. G., et al. (2021). Patterns of post-drought recovery are strongly influenced by drought duration, frequency, post-drought wetness, and bioclimatic setting. *Global Change Biol.* **27**:4630–4643. DOI:10.1111/gcb.15788
77. Liang Y., Wang J., Hao Z., et al. (2026). Anthropogenically-driven escalating impact of soil-based compound dry-hot extremes on vegetation productivity. *Nat. Commun.* **17**:2303. DOI:10.1038/s41467-026-68878-3
78. Guan Y., Gu X., Dai A., et al. (2025). Anthropogenic enhancement of subsurface soil moisture droughts. *Nat. Clim. Change* **15**:1355–1362. DOI:10.1038/s41558-025-02458-z
79. Allen C. D., Macalady A. K., Chenchouni H., et al. (2010). A global overview of drought and heat-induced tree mortality reveals emerging climate change risks for forests. *For. Ecol. Manage.* **259**:660–684. DOI:10.1016/j.foreco.2009.09.001

FUNDING AND ACKNOWLEDGMENTS

S. H. acknowledges the supports from the Postdoctoral Fellowship Program and China Postdoctoral Science Foundation under Grant Number BX20250027 and a grant from State Key Laboratory of Resources and Environmental Information System, Institute of Geographic Sciences and Natural Resources Research, Chinese Academy of Sciences. N. C. acknowledges the financial supports from the National Key Research and Development Program of China (2024YFB3908600) and the Key Research and Development Program of Hubei Province program (2023BCA003). J. G. acknowledges the financial support from the National Natural Science Foundation of China program (42090010). C. W. acknowledges the financial support from the National Key Research and Development Program of China (2023YFC3209101) and Natural Science Foundation of Hubei Province (2024AFB551). S. W. acknowledges the financial support from the Natural Science Foundation of China program (42401554) and the Natural Science Foundation of Hubei Province of China (2024AFB061). The numerical calculations in this paper have been conducted on the supercomputing system in the Supercomputing Center of Wuhan University. The funders had no role in study design, data collection and analysis, decision to publish, or preparation of the manuscript.

AUTHOR CONTRIBUTIONS

S. H. contributed to the conceptualization, methodology, software, formal analysis, and writing (original draft) of the manuscript. S. W., J. G., and N. C. contributed to the conceptualization, methodology, funding acquisition, supervision, and review & editing of the manuscript. X. Z., C. W., and S. W. contributed to the conceptualization and review & editing of the manuscript. All authors contributed to the manuscript and approved the final version.

DECLARATION OF INTERESTS

The authors declare no competing interests.

DATA AND CODE AVAILABILITY

BEPS-GPP data can be accessed at https://www.nesdc.org.cn/sdo/detail?id=612f42ee7e28172cbed3d809. MODIS-GPP data can be accessed at https://cmr.earthdata.nasa.gov/search/concepts/C2764707175-ORNL_CLOUD.html. GOSIF-GPP data can be accessed at https://data.globalecology.unh.edu/data/GOSIF-GPP_v2/. VOD-GPP data can be accessed at https://researchdata.tuwien.ac.at/records/1k7aj-bdz35.NIRv-GPP data can be accessed at https://data.tpdc.ac.cn/en/data/d6dff40f-5dbd-4f2d-ac96-55827ab93cc5/. ERA5-Land data can be accessed at https://cds.climate.copernicus.eu/datasets/reanalysis-era5-land?tab=overview. CMIP6 simulation data can be accessed at https://esgf-node.ipsl.upmc.fr/search/cmip6-ipsl/. MCD12Q1 products can be accessed at https://lpdaac.usgs.gov/products/mcd12q1v006/. Köppen climate classification product is provided by https://www.gloh2o.org/koppen. Classification of arid zones can be downloaded at https://data.tpdc.ac.cn/en/data/86e5f363-5044-4116-b73f-6e218988b241. Additional code and data related to this paper are available from the corresponding authors upon reasonable request.

SUPPLEMENTAL INFORMATION

It can be found online at https://doi.org/10.59717/j.xinn-geo.2026.100235.